Z. Phys. C – Particles and Fields 47, 167–179 (1990)

Zeitschrift für Physik C Particles and Fields


# Strange meson production in $e^+ e^-$ annihilation

TASSO Collaboration

W. Braunschweig, R. Gerhards, F.J. Kirschfink[1], H.-U. Martyn

I. Physikalisches Institut der RWTH, Aachen, Federal Republic of Germany[a]

H.M. Fischer, H. Hartmann, J. Hartmann, E. Hilger, A. Jocksch, R. Wedemeyer

Physikalisches Institut der Universität, Bonn, Federal Republic of Germany[a]

B. Foster, A.J. Martin

H.H. Wills Physics Laboratory, University of Bristol, Bristol, UK[b]

F. Barreiro[2], E. Bernardi[3], J. Chwastowski[4], A. Eskreys[4], K. Gather, K. Genser[5], H. Hultschig, P. Joos, H. Kowalski[6], A. Ladage, B. Löhr, D. Lüke[7], P. Mättig[8], D. Notz, J.M. Pawlak[5], K.-U. Pösnecker, E. Ros, D. Trines, R. Walczak[5], G. Wolf

Deutsches Elektronen-Synchrotron DESY, Hamburg, Federal Republic of Germany

H. Kolanoski

Physikalisches Institut, Universität, Dortmund, Federal Republic of Germany[a]

T. Kracht[9], J. Krüger, E. Lohrmann, G. Poelz, W. Zeuner[10]

II. Institut für Experimentalphysik der Universität, Hamburg, Federal Republic of Germany[a]

J. Hassard, J. Shulman, D. Su[11], I. Tomalin, A. Watson

Department of Physics, Imperial College, London, UK[b]

G. Cases[12], L. Hervas[13], A. Leites[13], J. del Peso, J. Fdez. de Trocóniz

Universidad Autonoma de Madrid, Madrid, Spain[c]

M.G. Bowler, P.N. Burrows[14], R. Cashmore, M.E. Veitch

Department of Nuclear Physics, Oxford University, Oxford, UK[b]

J.C. Hart, D.H. Saxon

Rutherford Appleton Laboratory, Chilton, Didcot, UK[b]

S. Brandt, M. Holder, L. Labarga[15]

Fachbereich Physik der Universität-Gesamthochschule, Siegen, Federal Republic of Germany[a]

Y. Eisenberg, U. Karshon, G. Mikenberg, A. Montag, D. Revel, E. Ronat, A. Shapira, N. Wainer, G. Yekutieli

Weizmann Institute, Rehovot, Israel[d]

A. Caldwell[16], D. Muller[17], S. Ritz[16], D. Strom[18], M. Takashima[10], Sau Lan Wu, G. Zobernig

Department of Physics, University of Wisconsin, Madison, WI, USA[e]

Received 28 November 1989

[1] Now at Lufthansa, Hamburg, FRG
[2] Alexander v. Humboldt Fellow, on leave from Universidad Autonoma de Madrid
[3] Now at Robert Bosch GmbH, Schwieberdingen, FRG
[4] Now at Inst. of Nuclear Physics, Cracow, Poland
[5] Now at Warsaw University[f], Poland
[6] On leave at Columbia University, NY, USA
[7] On leave at CERN, Geneva, Switzerland
[8] Now at IPP Canada, Carleton University, Ottawa, Canada
[9] Now at Hasylab, DESY, Hamburg, FRG
[10] Now at CERN, Geneva, Switzerland
[11] Now at Rutherford Appleton Laboratory, UK
[12] Supported by a grant from Banco Exterior de España
[13] Partially supported by DGICIT (Spain) and Kfz-Karlsruhe (Germany)
[14] Now at MIT, Cambride, Mass., USA
[15] Now at University of California at Santa Cruz, CA, USA
[16] Now at Columbia University, NY, USA
[17] Now at SLAC, California, CA, USA
[18] Now at University of Chicago, Chicago, IL, USA

[a] Supported by Bundesministerium für Forschung und Technologie
[b] Supported by UK Science and Engineering Research Council
[c] Supported by CAICYT
[d] Supported by the Minerva Gesellschaft für Forschung GmbH
[e] Supported by US Dept. of Energy, contract DE-AC02-76ER000881 and by US Nat. Sci. Foundation Grant no INT-8313994 for travel
[f] Partially supported by grant CPBP 01.06

**Abstract.** The full TASSO data have been used to study the inclusive production of strange mesons in $e^+e^-$ annihilations. Differential and total cross sections have been measured in the centre of mass energy range 14 to 44 GeV for $K^0$, $\bar{K}^0$ and 34.5 to 44 GeV for $K^{*\pm}(892)$. We have investigated the strange meson production properties in jets by studying the rapidity and $p_t^2$ distributions as well as the evolution of the multiplicities as a function of the event sphericity. We find no evidence that the strange meson yields increase with increasing sphericity faster than the total charged multiplicity.

## 1 Introduction

Hadron production in $e^+e^-$ annihilation is understood as the result of the production and subsequent decay of a quark-antiquark pair. This decay is a two step process. In the first step, the primary $q\bar{q}$ pair radiates colour and energy, giving rise to a parton cascade. In the second step, which takes place when these quanta have reached masses below a certain cut-off, the radiated quarks and gluons condense into colourless hadrons. It is generally accepted that these two processes can be described by QCD, however in two very different regimes [1, 2]. While the parton cascade development is of a perturbative nature, the way quarks and gluons metamorphose themselves into hadrons is clearly non-perturbative. Thus, while the former is calculable, the latter can at best be modelled.

Measurements of inclusive particle production cross-sections as a function of their quark and spin configurations are considered to provide insight into our understanding of the fragmentation process. In this context, the aim of the present paper is twofold [3]. On one hand we extend previous measurements on $K^0(\bar{K}^0)$ production characteristics at 14, 22 and 34 GeV [4] up to centre of mass energies of 46.7 GeV. On the other hand we also present data on $K^{*\pm}$ production through its decay mode $K_s^0\pi^\pm$, where the $K_s^0$ is identified by its weak $\pi^+\pi^-$ decay. Data on strange baryon production have been published separately [5].

## 2 $K^0$ Analysis

### 2.1 Experimental details

The experiment was performed at the $e^+e^-$ storage ring PETRA. The data sample used for this analysis corresponds to an integrated luminosity of 198.4 $pb^{-1}$. The luminosity was determined by measuring small and wide angle Bhabha scattering. The systematic error affecting the luminosity determination is 3%. The data was collected with the TASSO detector at c.m. energies $\sqrt{s}$ = 14.8, 21.5, 34.5, 35 and 42.6 GeV. The characteristics of each subset are shown in Table 1. The first three samples were taken with the early TASSO configuration [6], in which the central detector consisted of a central proportional chamber (CPC) surrounded by a large drift chamber (CDC). Tracks were reconstructed from the hits in these two chambers using a track finder known as MILL [7]. The remaining two samples were taken after the installation of a vertex detector (VXD) [8]. To make use of the VXD information, we employed a track finder known as PASS5 [9]. This extrapolated each MILL track into the VXD and attempted to associate VXD hits with it. In order to ensure that tracks were reliably reconstructed in the VXD, PASS5 tracks were only retained if they have hits assigned to them in at least four of the eight layers of the VXD. For the purpose of the current analysis, if PASS5 failed to extend a particular MILL track into the VXD, then we just used the MILL track for the analysis instead.

**Table 1.** Characteristics of the event samples used in this analysis

| Sample | $\langle\sqrt{s}\rangle$ (GeV²) | Events | $\mathscr{L}$ ($nb^{-1}$) | $K_s^0$ candidates | Background |
|---|---|---|---|---|---|
| 1 | 14.8 | 2921 | 1757 | 396 | 39 |
| 2 | 21.5 | 1921 | 2872 | 292 | 55 |
| 3 | 34.5 | 22725 | 78178 | 3426 | 289 |
| 4 | 35.0 | 31339 | 111203 | 4766 | 175 |
| 5 | 42.6 | 8447 | 4403 | 1262 | 90 |

The analysis procedures for selecting hadronic annihilation events have been described elsewhere [10]. In particular, the $e^+e^-$ interaction point, to which we will often refer as the primary vertex, was taken at the centre of the beam spot, as determined from tracks accumulated during several hours of running. For details we refer the reader to [11].

To isolate the sample of charged particle track pairs from the long lived decays $K_s^0 \to \pi^+\pi^-$, conditions were placed upon both individual charged particle tracks and upon track pairs. The individual track conditions were: i) the cosine of the production angle of the track relative to the beam is less than 0.87 in magnitude, ii) the momentum component in the plane perpendicular to the beam axis, the $x-y$ plane, is greater than 100 MeV/c, iii) $d_0$, defined to be the distance of the closest approach in the $x-y$ plane with respect to the primary vertex, is greater than 0.2 cm when the track had no vertex chamber hits, and greater than 0.1 cm when it did, iv) the track passes within 20 cm of the intersection point in the $z$ direction.

The algorithm for finding vertices began with a systematic pairing of all oppositely charged particle tracks. The two intersection points in the $x-y$ plane were calculated as candidate secondary vertices and each was subject to the following criteria: i) The tracks must have no vertex drift-chamber hits between the primary and the secondary vertices or missing hits after the secondary. ii) The angle between the particle's momentum direction and the line connecting the primary and secondary vertices is less than 15°. iii) The reconstructed impact parameter of the $K_s^0$ at the primary vertex must be less than 0.5 cm. iv) The invariant mass considering the two tracks to be electrons is required to be greater than

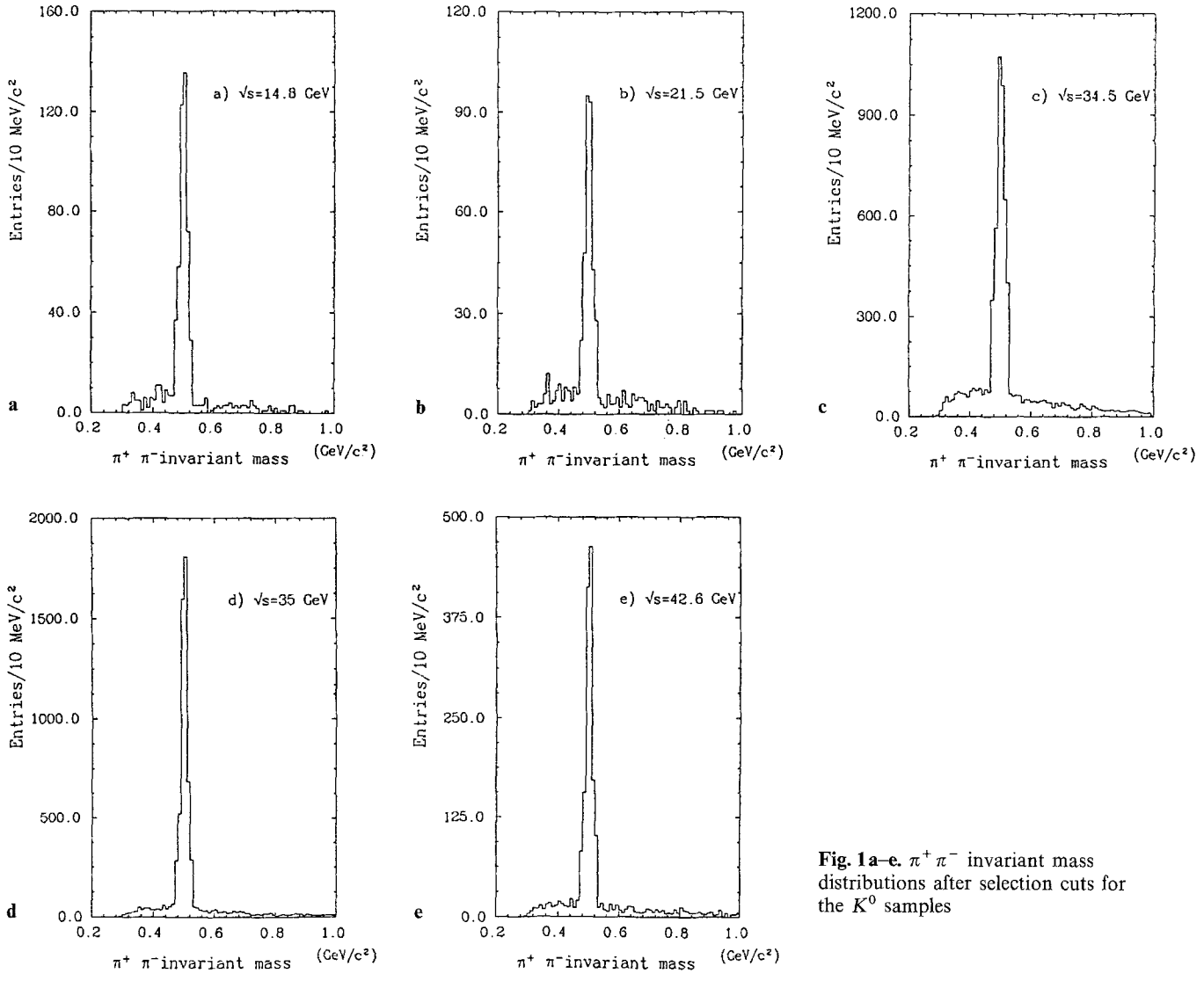


**Fig. 1a–e.** $\pi^+\pi^-$ invariant mass distributions after selection cuts for the $K^0$ samples

100 MeV/c$^2$. v) The distance in the $x-y$ plane from primary to secondary vertex is greater than 0.5 cm.

For all candidates a 3-dimensional vertex fit was performed [12]. The resulting $\pi^+\pi^-$ invariant mass distributions are shown in Fig. 1. The $K_s^0$ mass distributions integrated over all momenta have standard deviations of 18 and 12 MeV/c$^2$ for the pre and post VXD data respectively. The number of $K_s^0 \to \pi^+\pi^-$ candidates in the mass range 0.478 to 0.518 GeV/c$^2$ for combinations with a momentum lower than 2 GeV/c, or in the range 0.468 to 0.528 GeV/c$^2$ if it is greater than 2 GeV/c, are given in Table 1. The background shape in each case was obtained using pion pairs from the mass intervals 0.430 to 0.450 GeV/c$^2$ and 0.550 to 0.570 GeV/c$^2$. The acceptance corrections and the detection efficiencies were calculated from a complete parallel analysis using Monte Carlo techniques with full detector simulation [13]. The resulting efficiency curves at 35 GeV are shown in Fig. 2 for both samples i.e. with and without vertex detector. For completeness we also show the efficiency curve obtained in our previous publication [4] prior to the installation of the VXD and where no use was made of the

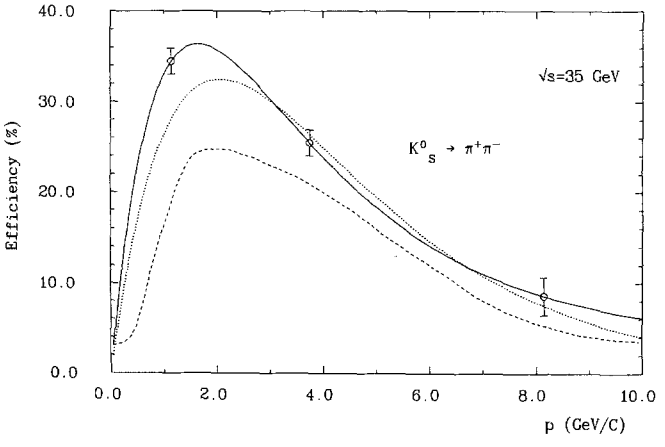


**Fig. 2.** The $K^0$ reconstruction efficiency as a function of momentum at $\sqrt{s}=35$ GeV. The dashed line corresponds to the old TASSO configuration without VXD, no three dimensional vertex fit. The dotted line illustrates the improvement due to including a three dimensional vertex fitting. The solid line shows the gain obtained with both VXD and three dimensional vertex fitting. The error bars illustrate the uncertainty in the determination of the detection efficiency at three particular momentum regions

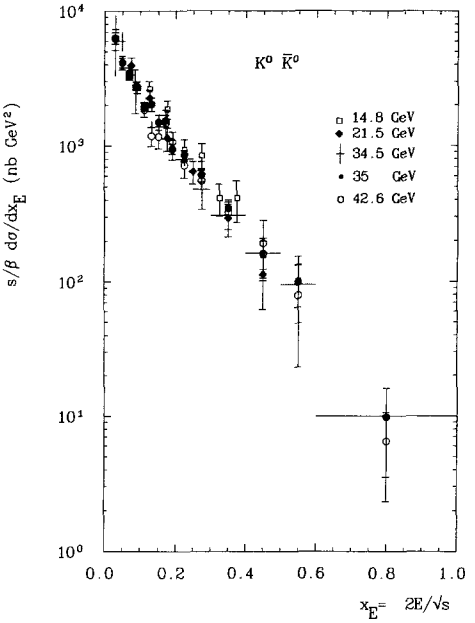


**Fig. 3.** The scaled cross section $(s/\beta)\,d\sigma/dx_E$ at $\sqrt{s}=14.8$, 21.5, 34.5, 35 and 42.6 GeV for $K^0$

3-dimensional vertex fitting. Notice that our overall efficiency has improved by approximately a factor 2.

Radiative corrections were taken into account on a bin by bin basis following standard Monte Carlo procedures. To this purpose the Berends-Kleiss [14] generator for initial state radiation was implemented in the Monte Carlo programs mentioned above.

In order to estimate systematic errors affecting the cross section determinations, two different Monte Carlo generators were used, namely the independent jet fragmentation (Hoyer) [15] and the string type (Lund) [16]. The results are included in the systematic errors that we will quote later on. Notice that compared to our previous analysis [4] we have been able to reduce the systematic errors by approximately a factor of 2. This is mainly due to our much improved efficiency, and to a less extent to a better understanding of the detector as well as to higher statistics.

The separation of signal and background events was performed by weighting according to the formula [17]

$$w(x)=\frac{s(x)}{s(x)+A\cdot b(x)} \quad \text{with } A=\frac{N_B}{N_S}, \tag{1}$$

where $s(x)$ and $b(x)$ are the expected (normalized) distributions for the signal and background (calculated by Monte Carlo methods), and $N_S$ and $N_B$ are the event numbers. To be sensitive to the systematic error of the signal-background separation, we used as $x$ variable the momentum and the fractional energy $x_E=2E/\sqrt{s}$ of the candidates.

### 2.2 *Differential cross sections*

Figure 3 and Table 2 show the scaled differential cross sections $(s/\beta)(d\sigma/dx_E)$ for the $K^0$ and $\bar{K}^0$. The data are

**Table 2a, b.** Scaled cross section, $(s/\beta)\,d\sigma/dx_E$ for $K^0$ production at various c.m. energies in $\mu b\cdot GeV^2$. The errors quoted are the quadratic sum of the statistical and systematic errors

**a**

| $x_E$ | $(s/\beta)\,d\sigma/dx_E$ | | |
|---|---|---|---|
| | $\sqrt{s}=42.6$ GeV | $\sqrt{s}=35$ GeV | $\sqrt{s}=34.5$ GeV |
| 0.02–0.04 | 6.22 ±1.08 | 6.33 ±0.60 | 6.32 ±1.40 |
| 0.04–0.06 | 4.14 ±0.48 | 4.13 ±0.35 | 6.00 ±0.95 |
| 0.06–0.08 | 3.48 ±0.32 | 3.31 ±0.24 | 3.57 ±0.35 |
| 0.08–0.10 | 2.72 ±0.27 | 2.76 ±0.19 | 2.68 ±0.29 |
| 0.10–0.12 | 1.84 ±0.22 | 1.94 ±0.14 | 1.95 ±0.17 |
| 0.12–0.14 | 1.18 ±0.19 | 2.02 ±0.24 | 1.37 ±0.14 |
| 0.14–0.16 | 1.16 ±0.21 | 1.49 ±0.19 | 1.46 ±0.24 |
| 0.16–0.18 | 1.48 ±0.35 | 1.53 ±0.15 | 1.53 ±0.18 |
| 0.18–0.20 | 1.06 ±0.20 | 0.94 ±0.16 | 1.03 ±0.13 |
| 0.20–0.25 | 0.72 ±0.14 | 0.86 ±0.07 | 0.79 ±0.08 |
| 0.25–0.30 | 0.55 ±0.21 | 0.61 ±0.07 | 0.48 ±0.06 |
| 0.30–0.40 | 0.32 ±0.08 | 0.35 ±0.04 | 0.31 ±0.04 |
| 0.40–0.50 | 0.19 ±0.09 | 0.16 ±0.04 | 0.16 ±0.04 |
| 0.50–0.60 | 0.079±0.056 | 0.106±0.034 | 0.095±0.013 |
| 0.60–1.00 | 0.016±0.041 | 0.010±0.003 | 0.012±0.010 |

**b**

| $\sqrt{s}=14.8$ GeV | | $\sqrt{s}=21.5$ GeV | |
|---|---|---|---|
| $x_E$ | $(s/\beta)\,d\sigma/dx_E$ | $x_E$ | $(s/\beta)\,d\sigma/dx_E$ |
| 0.07–0.10 | 3.05 ±0.97 | 0.05–0.10 | 3.94±0.59 |
| 0.10–0.15 | 2.74 ±0.36 | 0.10–0.15 | 2.25±0.34 |
| 0.15–0.20 | 1.86 ±0.29 | 0.15–0.20 | 1.13±0.22 |
| 0.20–0.25 | 0.94 ±0.17 | 0.20–0.30 | 0.64±0.12 |
| 0.25–0.30 | 0.85 ±0.19 | 0.30–0.40 | 0.29±0.08 |
| 0.30–0.35 | 0.41 ±0.11 | 0.40–0.50 | 0.11±0.05 |
| 0.35–0.40 | 0.41 ±0.14 | | |
| 0.40–0.50 | 0.16 ±0.05 | | |
| 0.50–0.60 | 0.101±0.052 | | |

in agreement with our previous measurements [4, 18, 19] and with results from the PETRA and PEP experiments JADE [20], PLUTO [21] and CELLO [22], MARK II [23], HRS [24] and TPC [25]. The data show scaling violation effects, however the size is smaller than that previously published [4]. We attribute this effect to improvements in the $V_0$ finding algorithm and the detector simulation programs as well as to our increased statistics. In order to have a closer look at the scaling violation effects we plot in Fig. 4 the $K^0$ production cross-sections as a function of centre of mass energy for three intervals in $x_E$. These data have been fitted to the expression [26]

$$\frac{s}{\beta}\frac{d\sigma}{dx_E}=a\left(1+b\ln\frac{s}{s_0}\right) \tag{2}$$

where $s_0$ is a reference scale set to 1 GeV$^2$. The parameter $b$ is a measure of the scaling violating effects, the resulting values being $-0.090\pm0.009$, $-0.064\pm0.027$ and $-0.018\pm0.085$, respectively, for the three intervals in $x_E$ shown in Fig. 4.

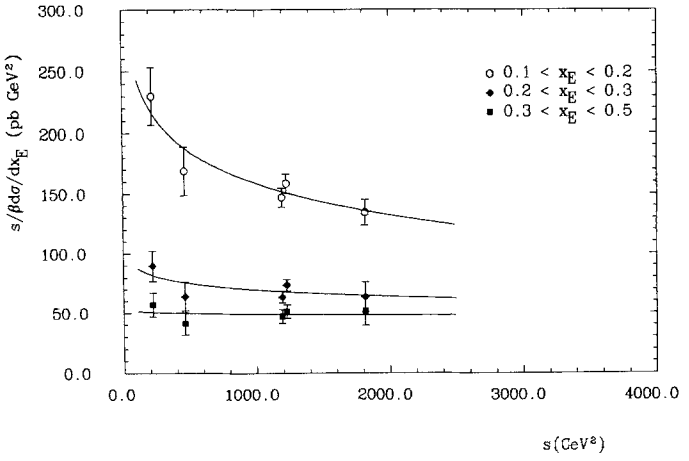


**Fig. 4.** The inclusive spectra $(s/\beta)d\sigma/dx_E$ for different $x_E$ bins as a function of c.m. energy

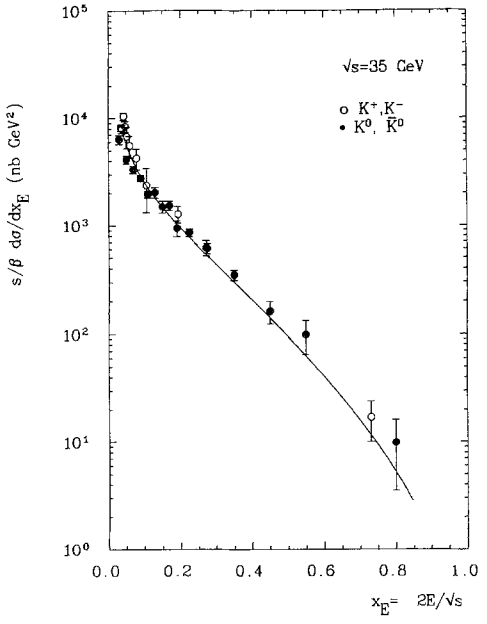


**Fig. 5.** The scaled cross section $(s/\beta)d\sigma/dx_E$ (μb GeV$^2$) at $\sqrt{s}$ = 35 GeV for $K^0\bar{K}^0$ and $K^{\pm}$ together with Lund model prediction for neutral kaon production

In Fig. 5 the scaling cross section for the charged [27] and neutral kaons at $\sqrt{s}=35$ GeV are shown together with the Lund expectation. All comparisons made in this paper between Lund and data, have been made using JETSET version 6.3 with the matrix elements option $O(\alpha_s^2)$. The quark production probabilities $P(qq)/P(q)$, $P(s)/P(u)$ and $\frac{P(us)/P(ud)}{P(s)/P(d)}$ were set to 0.10, 0.35 and 0.32 respectively, which were determined in one of our previous publications [4]. For $x_E>0.1$ the charged and neutral kaon scaling cross sections are in agreement with each other and with the Lund expectation. For $x_E<0.1$ the charged-kaon scaling cross section is bigger than that for the neutral kaons by a factor $\sim 1.4$ at $x_E$ $\sim 0.05$ with the Lund prediction falling in between the two.

**Table 3.** $K^0$ multiplicity, $R_{K^0}$, and integrated $K^0$ cross section

| $\langle\sqrt{s}\rangle$ | $\langle K^0\rangle$ | $R_{K^0}$ | $\sigma_{K^0}$ (pb) |
|---|---|---|---|
| 14.8 | $1.17\pm0.09\pm0.07$ | $4.69\pm0.36\pm0.31$ | $1861\pm140\pm122$ |
| 21.5 | $1.28\pm0.11\pm0.08$ | $5.13\pm0.44\pm0.36$ | $964\pm 82\pm 68$ |
| 34.5 | $1.49\pm0.04\pm0.05$ | $5.97\pm0.17\pm0.27$ | $436\pm 12\pm 20$ |
| 35 | $1.48\pm0.03\pm0.03$ | $5.93\pm0.13\pm0.21$ | $421\pm 9\pm 15$ |
| 42.6 | $1.52\pm0.05\pm0.05$ | $6.09\pm0.21\pm0.37$ | $292\pm 10\pm 18$ |

### *2.3 Integrated cross sections and $K^0$ multiplicity*

The total inclusive cross sections were obtained by integrating the differential cross sections. The branching ratio of $K^0\to\pi^+\pi^-$ was taken to be 34.3% [28]. Values for the total inclusive cross section relative to $\sigma_{pt}=4\pi\alpha^2/3s$ defined as

$$R_{K^0}=\frac{\sigma(e^+e^-\to K^0X)+\sigma(e^+e^-\to\bar{K}^0X)}{\sigma_{pt}}$$

are given in Table 3 for the five energies discussed so far, together with the $K^0$ multiplicities per hadronic event. The energy dependence of the $K^0$ cross sections is displayed in Fig. 6 along with a fit to the theoretical expectation [26]

$$\sigma=\frac{a}{s}\left(1+b\ln\frac{s}{s_0}\right). \tag{3}$$

Very good agreement between data and predictions is observed. The resulting values for the two free parame-

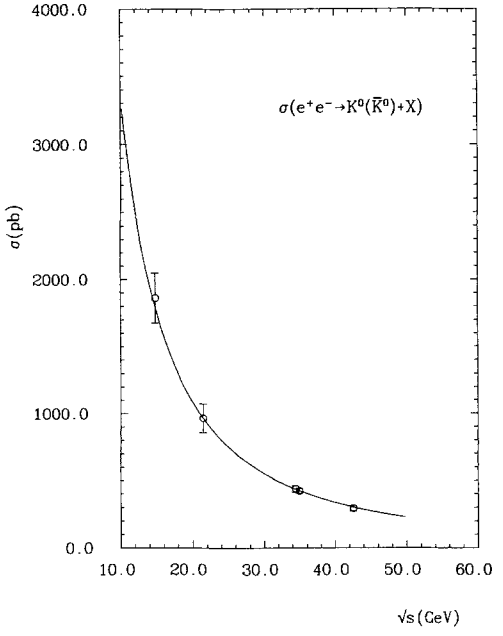


**Fig. 6.** $K^0$ production cross-section as a function of c.m. energy. The solid line represents the results of a fit discussed in the text

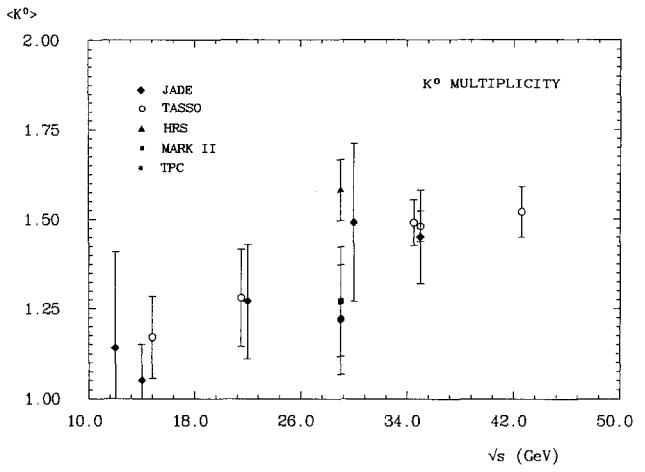


**Fig. 7.** $K^0$ multiplicity per hadronic event as a function of c.m. energy as measured by different experiments

ters in the fit are $a=1.45\pm0.04$ μb GeV$^2$ and $b=0.050\pm0.002$. The number of $K^0$ per hadronic event as a function of centre of mass energy are shown in Fig. 7, along with measurements by other experiments. They are also tabulated in Table 4. The logarithmic rise expected in QCD is observed, although other alternative functional dependences cannot be ruled out, because of the limited range in centre of mass energy.

### 2.4 $K^0$ production in jets

We have analyzed the $K^0$ production characteristics in the multiparticle final states originating from $e^+e^-$ annihilation in the centre of mass range 14 to 44 GeV. The kinematics for particles within jets are typically described using a transverse variable such as the $p_t^2$, and a longitudinal variable such as the rapidity $y$.

In this context, Fig. 8 shows the production cross section for $K^0$ as a function of the folded rapidity $y=\frac{1}{2}\ln\frac{E+|p_L|}{E-|p_L|}$, where $p_L$ is the momentum component parallel to the thrust axis of the event. The data displayed in Fig. 8 are compared to the expectations of the Lund Monte Carlo, and very good agreement is found. Each rapidity distribution exhibits a rather flat plateau, extending from $y=0$ approximately one unit of rapidity below the maximum value possible. Beyond this point the cross sections fall steeply. These distributions differ from those for all charged particles in two ways. First, the $K^0$ distributions are harder, in that the plateau extends further in rapidity. Secondly, the cross section near $y=0$ falls with increasing centre of mass energy, in contrast to what is observed for all charged particles. One important source of these differences is the contribution to the $K^0$ spectra of kaons from the decay of charmed particles which carry on average some 60% of the available energy. The decay products are concentrated within $\pm1$ unit of rapidity about the mean rapidity of the charmed particle. It is also relevant that the fragmentation function of kaons are harder than those for the less massive pions.

In Fig. 9 we show the $d\sigma/dp_t^2$ distributions for $K^0$ at centre of mass energies of 14.8, 21.5, 35 and 42.6 GeV. Here $p_t$ is the momentum component transverse to the sphericity axis of the event. At low $p_t^2$, $0.1<p_t^2<0.5$ (GeV/c)$^2$, they show an exponential fall off described by $Ae^{-p_t^2/2\sigma^2}$. The resulting values for $\sigma$ are found to be within our errors energy independent and range from $0.36\pm0.07$ GeV/c at 21.5 GeV to $0.33\pm0.02$ GeV/c at 35.0 GeV. At high energies the exponential fall-off at low transverse momenta, merges into a high transverse momentum tail. This indicates that the $K^0$ are produced both in three- and two-jet events.

Finally, in order to see whether the $K^0$ yields are different for these two topologies, we measured the $K^0$ multiplicity as a function of the event sphericity. The results of this analysis are presented in Table 5 and plotted in Fig. 10a together with the results of a parallel analysis for charged particles. We have also plotted in Fig. 10b the $K^0$ multiplicity relative to the total charged multiplicity as a function of sphericity together with the Lund expectation. We find no indication that the $K^0$ multiplicity per event increases with increasing event sphericity faster than the total charged multiplicity.

## 3 $K^*$ analysis

### 3.1 $K^*$ identification

Using the $K_s^0$ samples at the three highest energies discussed so far, we have searched for the decay

**Table 4.** $K^0$ multiplicity per hadronic event measured by PETRA and PEP experiments

| $\langle\sqrt{s}\rangle$ | TASSO | JADE | CELLO | TPC | MARK II | HRS |
|---|---|---|---|---|---|---|
| 12.0 | | $1.14\pm0.38$ | | | | |
| 14.0 | | $1.05\pm0.21$ | | | | |
| 14.8 | $1.17\pm0.09\pm0.07$ | | | | | |
| 22 | $1.28\pm0.11\pm0.08$ | $1.27\pm0.29$ | | | | |
| 29 | | | | $1.22\pm0.03\pm0.15$ | $1.27\pm0.03\pm0.15$ | $1.58\pm0.03\pm0.15$ |
| 30 | | $1.49\pm0.22\pm0.15$ | | | | |
| 34.5 | $1.49\pm0.04\pm0.05$ | $1.45\pm0.23$ | | | | |
| 35 | $1.47\pm0.03\pm0.05$ | | $1.42\pm0.09\pm0.18$ | | | |
| 42.6 | $1.52\pm0.05\pm0.05$ | | | | | |

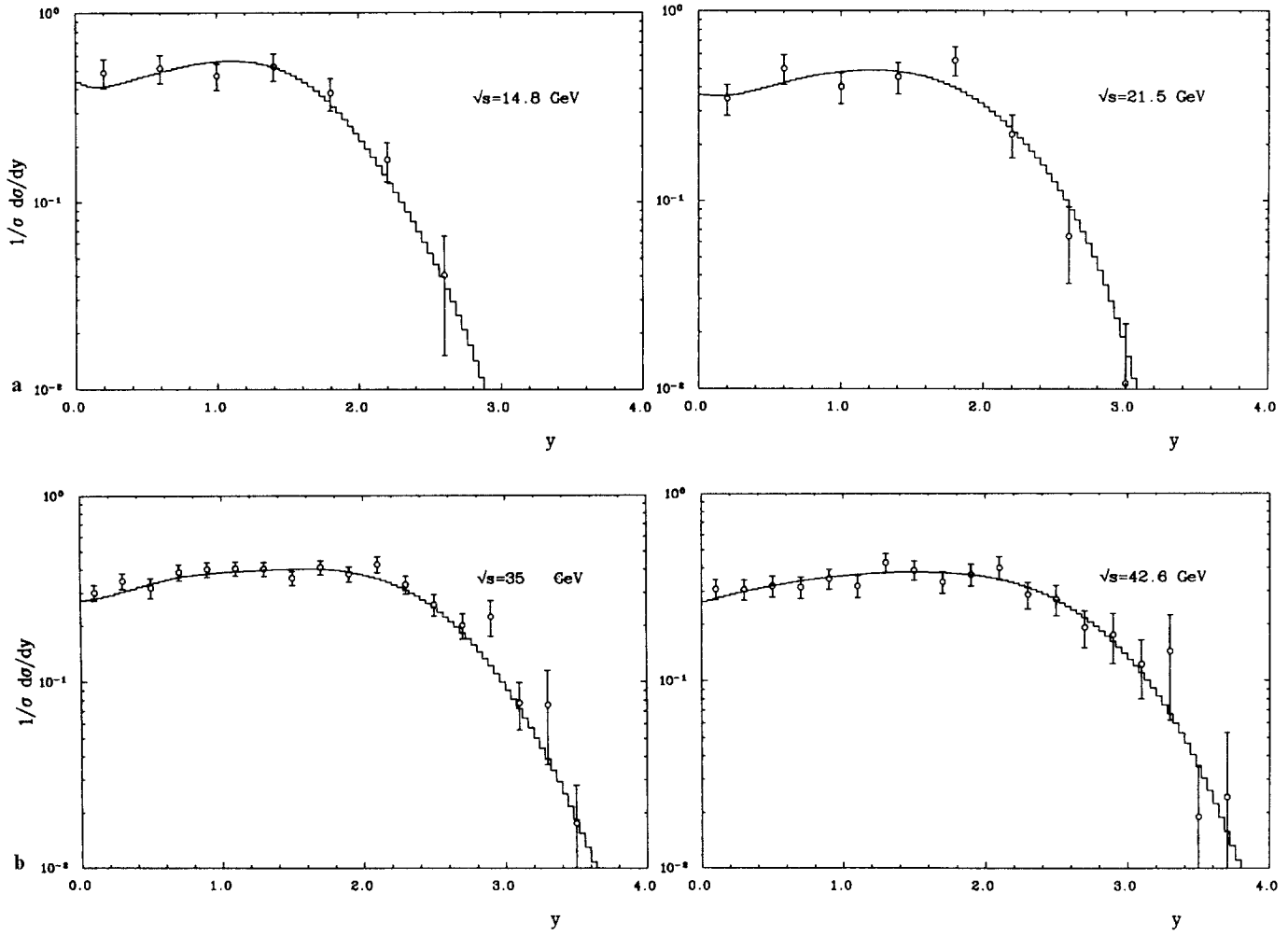


**Fig. 8.** $K^0$ rapidity distribution at $\sqrt{s}=14.8$, 21.5, 34.5, 35.0 and 42.6 GeV along with Lund expectations

$K^{*\pm}(892) \to K_s^0 \pi^\pm$. To this end $K_s^0$ were combined with any additional charged particle from the event vertex, using the pion hypothesis. In order to suppress background, the momentum of the additional pion was required to be greater than 0.1 GeV/c and the track had to belong to the same hemisphere, defined relative to the sphericity axis, as the $K_s^0$.

The resulting $K_s^0 \pi^\pm$ invariant mass distributions are plotted in Fig. 11. A clear enhancement, corresponding to the $K^{*\pm}(892)$ is seen. These mass spectra were fitted to the sum of a relativistic Breit-Wigner shape with the mass and width fixed to the known $K^{*\pm}(892)$ values [28], folded with the detector resolution, and a background. The results of the fits for each subset are listed in Table 6 together with the values of the mass and the width if they are left free.

In order to estimate the systematic errors coming from the fit, we have used three different expressions for the background:

$$f_1(x) = (x-m)^{\alpha_1} e^{-(\alpha_2 x + \alpha_3 x^2)}$$

$$f_2(x) = \left(\frac{x-m}{\sqrt{s}-m-\alpha_3}\right)^{\alpha_1} \left(1 - \frac{x-m}{\sqrt{s}-m-\alpha_3}\right)^{\alpha_2}$$

$$f_3(x) = \left(1 - e^{\frac{-(x-m)}{\alpha_1}}\right) e^{-(\alpha_2 x + \alpha_3 x^2)}$$

where the $\alpha_n$ are free parameters and $m$ is the $K^0\pi$ mass threshold. Since the $K_s^0$ were identified with relatively little background, it was not necessary to apply a cut in $x_E$ in order to suppress combinatorial background.

The acceptance corrections and detection efficiencies were calculated from a parallel analysis using Monte Carlo techniques as discussed in the previous section. Radiative corrections were also taken into account as described before. In order to estimate the systematic errors affecting our acceptance determinations two different fragmentation models were used as for the $K^0$ case.

### 3.2 *Differential cross sections*

The measured scaling cross section, $(s/\beta)(d\sigma/dx_E)$, as a function of the fractional energy is given in Table 7 and plotted in Fig. 12. In order to compare the scaling cross section of strange pseudoscalar mesons with strange vector mesons, we have plotted in Fig. 13 the scaling cross sections for $K^0$, $\bar{K}^0$, $K^\pm$ and for $K^{*\pm}(892)$. The spectra

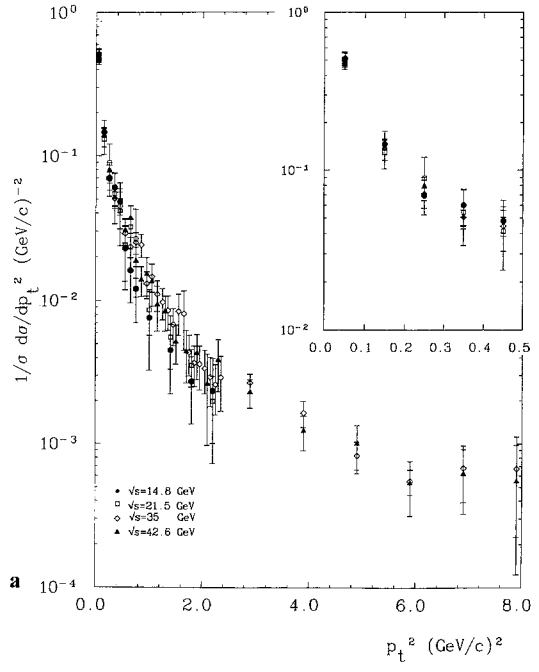


**Fig. 9. a** The $p_t^2$ distribution for $K^0$ production at $\sqrt{s}=14.8$, 21.5, 34.5, 35.0 and 42.6 GeV. The insert shows an enlarged view of the $p_t^2<0.5$ GeV$^2$ region. **b** The $p_t^2$ distribution for $K^0$ production at $\sqrt{s}=14.8$, 21.5, 34.5, 35.0 and 42.6 GeV, together with the Lund expectations

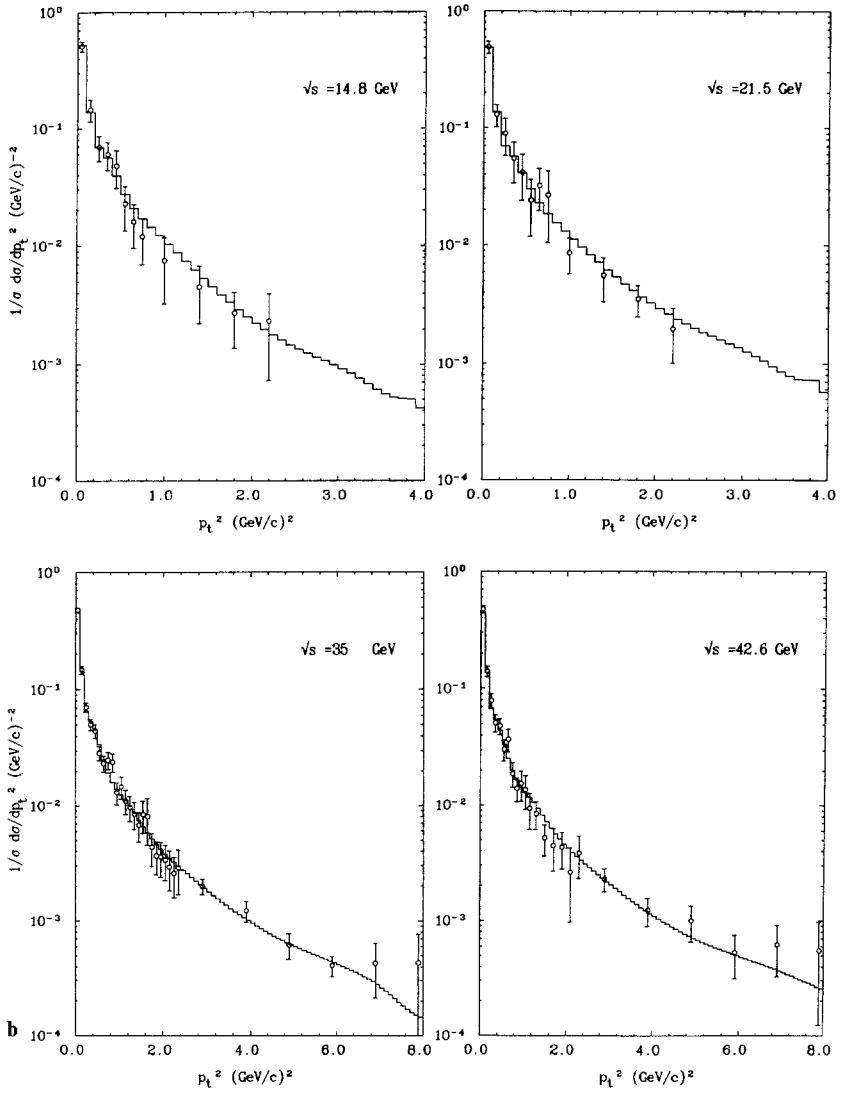

**Table 5a, b.** $K^0$ multiplicity as a function of event sphericity

**a**

| Sphericity | $\sqrt{s}=42.6$ GeV | | $\sqrt{s}=35$ GeV | |
|---|---|---|---|---|
| | $\langle K^0\rangle$ | $\langle K^0\rangle/\langle n_{Ch}\rangle$ | $\langle K^0\rangle$ | $\langle K^0\rangle/\langle n_{Ch}\rangle$ |
| 0.000–0.020 | $0.87\pm0.14$ | $0.083\pm0.015$ | $0.79\pm0.10$ | $0.082\pm0.012$ |
| 0.020–0.035 | $1.16\pm0.16$ | $0.089\pm0.013$ | $1.20\pm0.12$ | $0.099\pm0.011$ |
| 0.035–0.050 | $1.42\pm0.19$ | $0.103\pm0.015$ | $1.36\pm0.14$ | $0.106\pm0.012$ |
| 0.050–0.065 | $1.48\pm0.21$ | $0.100\pm0.016$ | $1.49\pm0.16$ | $0.108\pm0.013$ |
| 0.065–0.080 | $1.50\pm0.24$ | $0.098\pm0.017$ | $1.72\pm0.20$ | $0.120\pm0.016$ |
| 0.080–0.105 | $1.14\pm0.16$ | $0.072\pm0.011$ | $1.49\pm0.14$ | $0.100\pm0.011$ |
| 0.105–0.130 | $1.49\pm0.22$ | $0.091\pm0.015$ | $1.57\pm0.17$ | $0.103\pm0.013$ |
| 0.130–0.155 | $1.30\pm0.19$ | $0.064\pm0.013$ | $1.49\pm0.17$ | $0.096\pm0.013$ |
| 0.155–0.205 | $1.69\pm0.23$ | $0.100\pm0.015$ | $1.72\pm0.17$ | $0.110\pm0.013$ |
| 0.205–0.255 | $2.18\pm0.34$ | $0.121\pm0.022$ | $1.84\pm0.22$ | $0.111\pm0.015$ |
| 0.255–0.330 | $1.94\pm0.30$ | $0.108\pm0.019$ | $1.87\pm0.22$ | $0.111\pm0.015$ |
| 0.330–0.500 | $1.92\pm0.27$ | $0.107\pm0.017$ | $1.85\pm0.20$ | $0.111\pm0.014$ |
| 0.500–0.840 | $2.14\pm0.34$ | $0.115\pm0.026$ | $1.86\pm0.18$ | $0.132\pm0.023$ |

**b**

| $\sqrt{s}=14.8$ GeV | | | $\sqrt{s}=21.5$ GeV | | |
|---|---|---|---|---|---|
| Sphericity | $\langle K^0\rangle$ | $\langle K^0\rangle/\langle n_{Ch}\rangle$ | Sphericity | $\langle K^0\rangle$ | $\langle K^0\rangle/\langle n_{Ch}\rangle$ |
| 0.000–0.050 | $0.72\pm0.23$ | $0.116\pm0.040$ | 0.000–0.050 | $0.54\pm0.15$ | $0.123\pm0.050$ |
| 0.050–0.080 | $1.16\pm0.29$ | $0.147\pm0.041$ | 0.050–0.080 | $0.58\pm0.16$ | $0.163\pm0.049$ |
| 0.080–0.105 | $1.03\pm0.28$ | $0.116\pm0.034$ | 0.080–0.105 | $1.35\pm0.37$ | $0.145\pm0.044$ |
| 0.105–0.155 | $1.10\pm0.21$ | $0.120\pm0.026$ | 0.105–0.255 | $1.21\pm0.29$ | $0.147\pm0.050$ |
| 0.155–0.205 | $1.00\pm0.22$ | $0.104\pm0.025$ | 0.255–0.330 | $1.98\pm0.54$ | $0.147\pm0.051$ |
| 0.205–0.255 | $1.64\pm0.38$ | $0.162\pm0.042$ | 0.330–0.500 | $1.82\pm0.46$ | $0.161\pm0.051$ |
| 0.255–0.330 | $1.44\pm0.33$ | $0.133\pm0.034$ | 0.500–0.840 | $0.84\pm0.47$ | $0.151\pm0.050$ |
| 0.330–0.500 | $1.33\pm0.25$ | $0.122\pm0.026$ | | | |
| 0.500–0.840 | $1.43\pm0.33$ | $0.121\pm0.031$ | | | |

for pseudoscalar and vector kaons tend to each other at high $x_E$ values, however the former is much steeper than the latter. These features are will described by current fragmentation models. In fact the Lund curve shown in Fig. 12 which reproduces fairly well the data, was obtained with default values for the vector meson production probabilities. These probabilites were 50%, 60% and 75% for light, strange and heavy vector mesons, respectively.

### 3.3 *Integrated cross section and* $K^{*\pm}(892)$ *multiplicity*

The observed number of $K^{*\pm}(892)$ events, after corrections for the efficiency and the known branching ratios of its decay chain, resulted in the multiplicities given in Table 8. Note that we quote two errors, the first error is statistical while the second is systematic and reflects the uncertainties in the acceptance, the measured luminosity, and the background substraction. These multiplicities correspond to $R_{K^{*\pm}}$ values which are also listed in Table 8. These results are in reasonable agreement with the JADE [29] and CELLO [22] measurements of $0.87\pm0.16\pm0.08$ and $0.77\pm0.17\pm0.14$ respectively at $\sqrt{s}=35$ GeV and with the $0.62\pm0.06$ value of the HRS collaboration [30] at $\sqrt{s}=29$ GeV.

### 3.4 $K^{*\pm}(892)$ *production in jets*

We have investigated the $K^{*\pm}(892)$ production characteristics in jets for the sample at $\sqrt{s}=35$ GeV only, since the poor statistics of the other two samples precluded a similar analysis.

We show in Figs. 14 and 15 the rapidity and $p_t^2$ distributions. They exhibit a similiar behaviour to that shown for $K^0$. In particular the $p_t^2$ distribution shows again an exponential fall off at low transverse momenta, which can be fitted to the expression $Ae^{-p_t^2/2\sigma^2}$ yielding values for $\sigma$ compatible to that obtained for $K^0$ but with a larger error bar. Also as in the $K^0$ case, the data tend to flatten and develop a tail at large $p_t^2$ values. This is an indication that strange vector mesons are produced in three- as well as in two-jet events.

In analogy to our discussion in Sect. 2.4, we have investigated the evolution of the $K^{*\pm}(892)$ yield as a function of the event sphericity. These results are plotted in Fig. 16a. Figure 16b show the $K^{*\pm}(892)$ multiplicity relative to the total charged multiplicity as a function of sphericity. Although clearly the $K^{*\pm}(892)$ yield grows with increasing sphericity, we find no evidence that this increase is faster than for the total charged multiplicity. These results are summarized in Table 9. We remark that these results are stable upon relaxing the require-

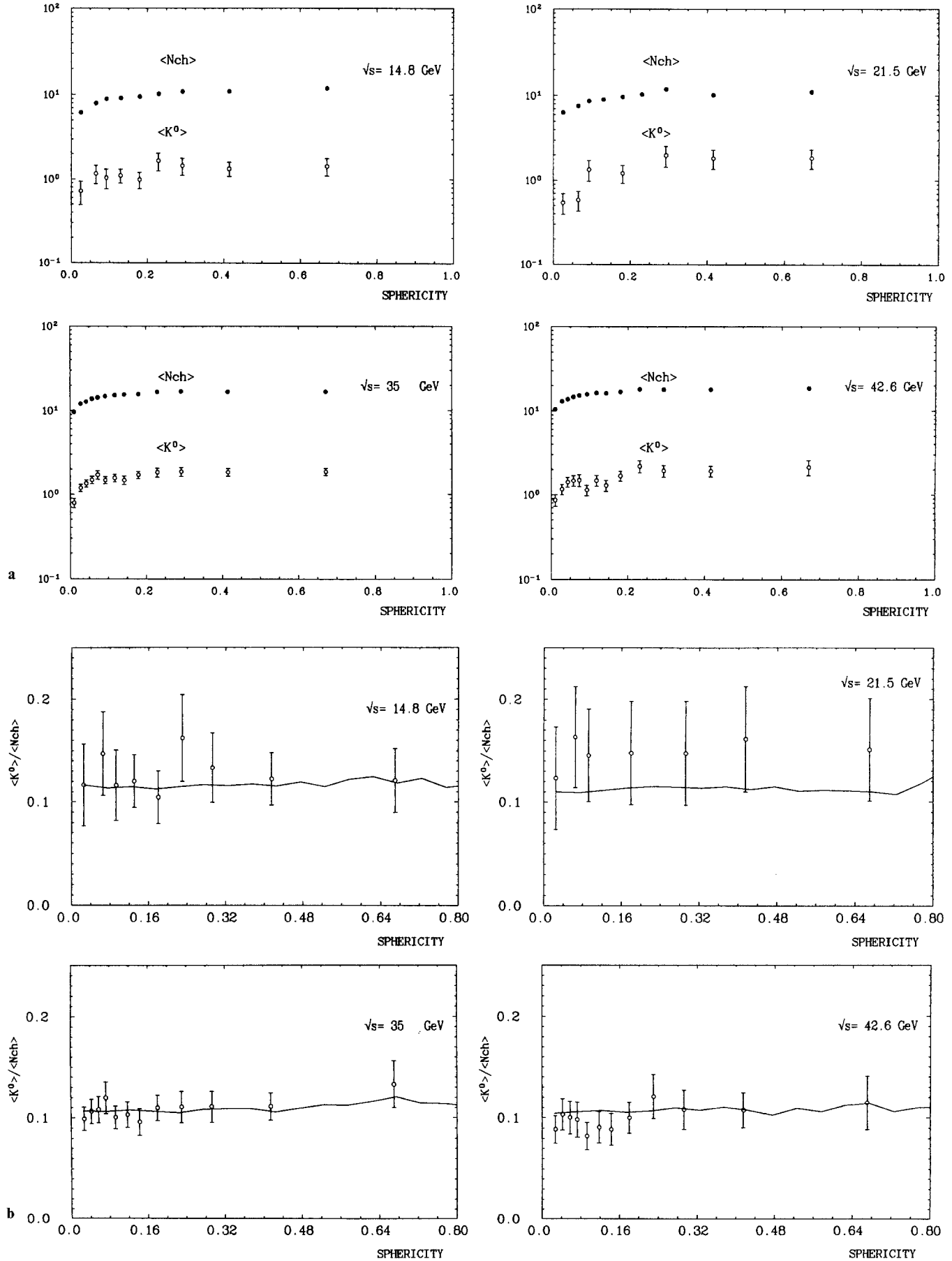


**Fig. 10.** **a** $K^0$ and total charged multiplicity as a function of event sphericity. **b** $K^0$ multiplicity relative to the total charged multiplicity as a function of event sphericity along with the prediction of the Lund Monte Carlo, solid line

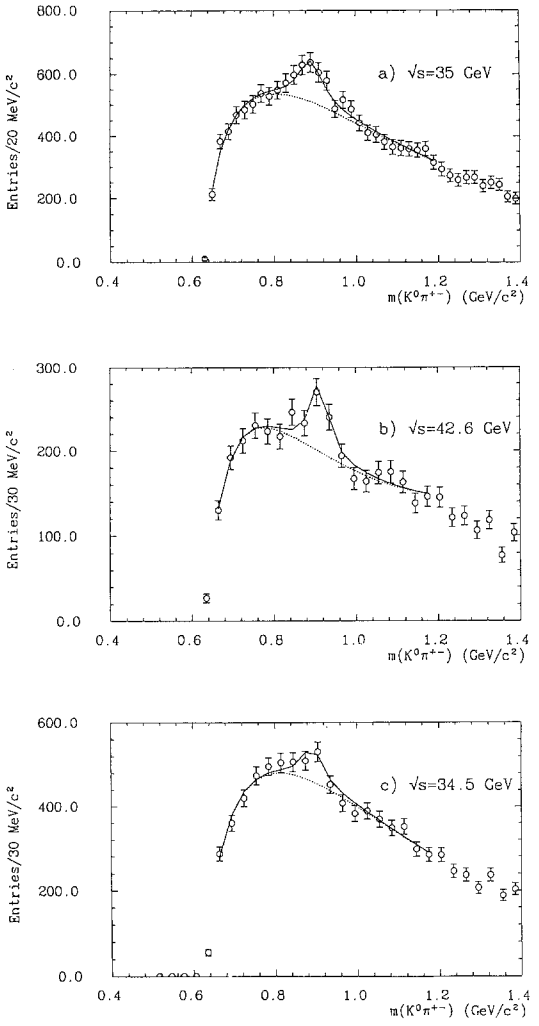


**Fig. 11a–c.** $K_s^0\pi^{\pm}$ invariant mass distributions at 34.5, 35 and 42.6 GeV

**Table 6.** Results of fits to the $K_s^0\pi$ mass distributions. The resulting number of $K^{*\pm}(892)$, as well as the fitted mass and width are given (in MeV)

| | $\sqrt{s}=34.5$ GeV | $\sqrt{s}=35.0$ GeV | $\sqrt{s}=42.6$ GeV |
|---|---|---|---|
| $\#K^{*\pm}$ | 219 ±77 ± 6 | 643 ±121 ±54 | 190 ±34 ±41 |
| $m_{K^*}$ | 893.0± 7.3± 7.4 | 889.7± 7.5±2.3 | 901.7±10.6± 1.1 |
| $\Gamma_{K^*}$ | 45.5± 8.1±22.4 | 60.2± 15.3±3.1 | 39.0± 9.0± 3.6 |

**Table 7.** Scaled cross section, $(s/\beta)\,d\sigma/dx_E$ in nb·GeV$^2$ for $K^{*\pm}(892)$ production

| $x_E$ | $(s/\beta)\,d\sigma/dx_E$ | | |
|---|---|---|---|
| | $\sqrt{s}=42.6$ GeV | $\sqrt{s}=35$ GeV | $\sqrt{s}=34.5$ GeV |
| 0.05–0.10 | 1850±962±275 | 1193±689±175 | 1870±853±278 |
| 0.10–0.20 | 815±352± 80 | 844±215±139 | 842±378± 90 |
| 0.20–0.40 | 250±131± 75 | 237± 85± 20 | 253±114± 39 |
| 0.40–0.80 | 141± 47± 74 | 73± 28± 14 | 52± 34± 6 |

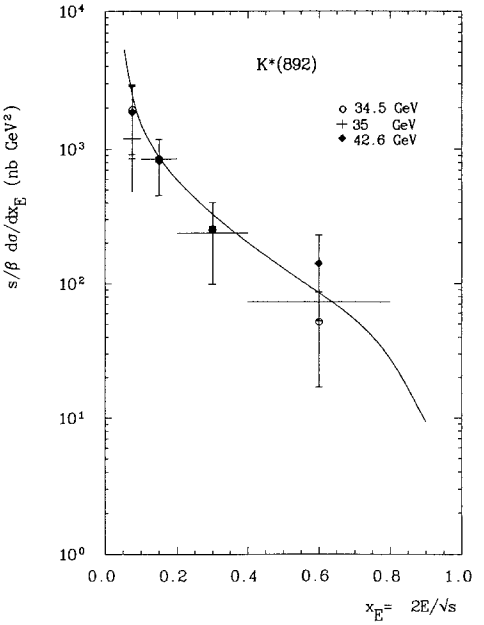


**Fig. 12.** The scaled cross section $(s/\beta)\,d\sigma/dx_E$ at $\sqrt{s}=42.6$, 35 and 34.5 GeV for $K^{*\pm}(892)$ production along with the expectation from the Lund Monte Carlo at $\sqrt{s}=35$ GeV

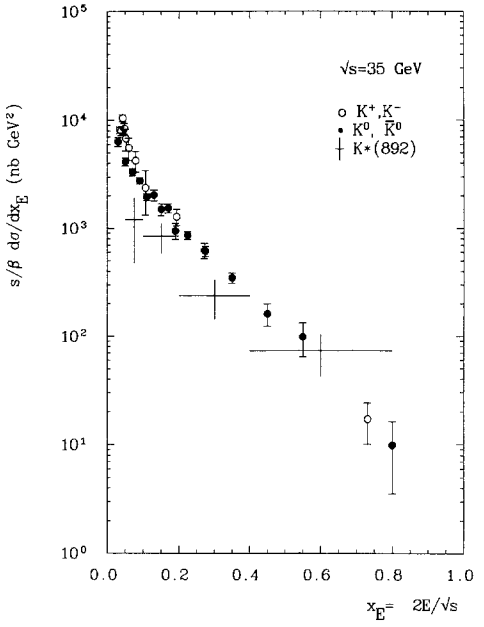


**Fig. 13.** The scaled cross sections for strange pseudoscalar and vector mesons production

**Table 8.** $K^{*\pm}(892)$ multiplicity, $R_{K^{*\pm}}$, and integrated $K^{*\pm}$ cross section

| $\langle\sqrt{s}\rangle$ | $\langle K^{*\pm}\rangle$ | $R_{K^{*\pm}}$ | $\sigma_{K^{*\pm}}$ (pb) |
|---|---|---|---|
| 34.5 | 0.51±0.18±0.07 | 2.04±0.72±0.27 | 148.9±52.6±20 |
| 35 | 0.66±0.12±0.04 | 2.53±0.48±0.21 | 179.5±34.1±15 |
| 42.6 | 0.77±0.17±0.08 | 3.09±0.68±0.37 | 147.8±32.6±18 |

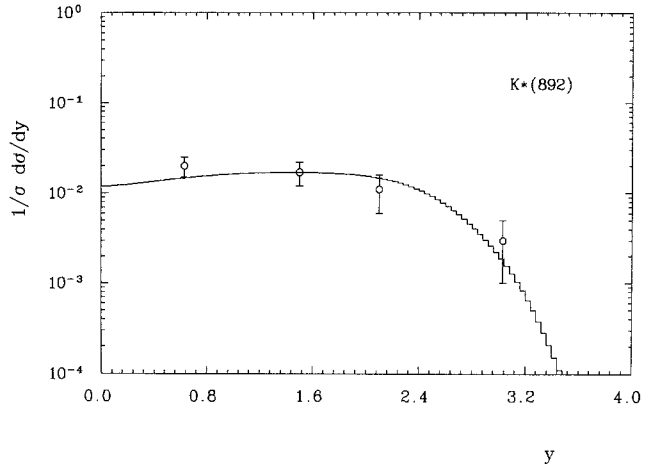


**Fig. 14.** $K^{*\pm}(892)$ rapidity distribution at $\sqrt{s}=35.0$ GeV together with the Lund prediction

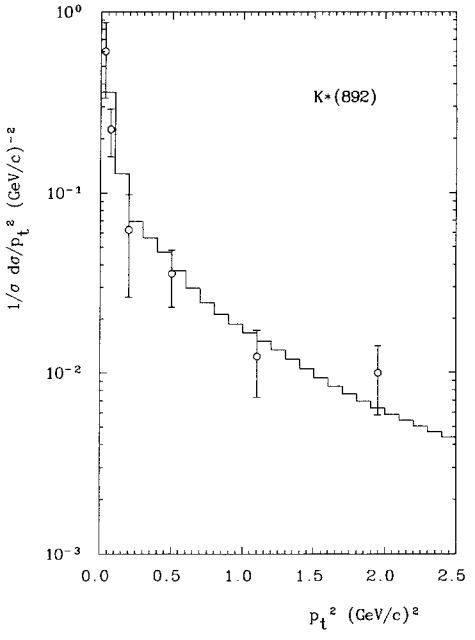


**Fig. 15.** The $p_t^2$ distributions for $K^{*\pm}(892)$ production at $\sqrt{s}=35.0$ GeV together with the Lund prediction

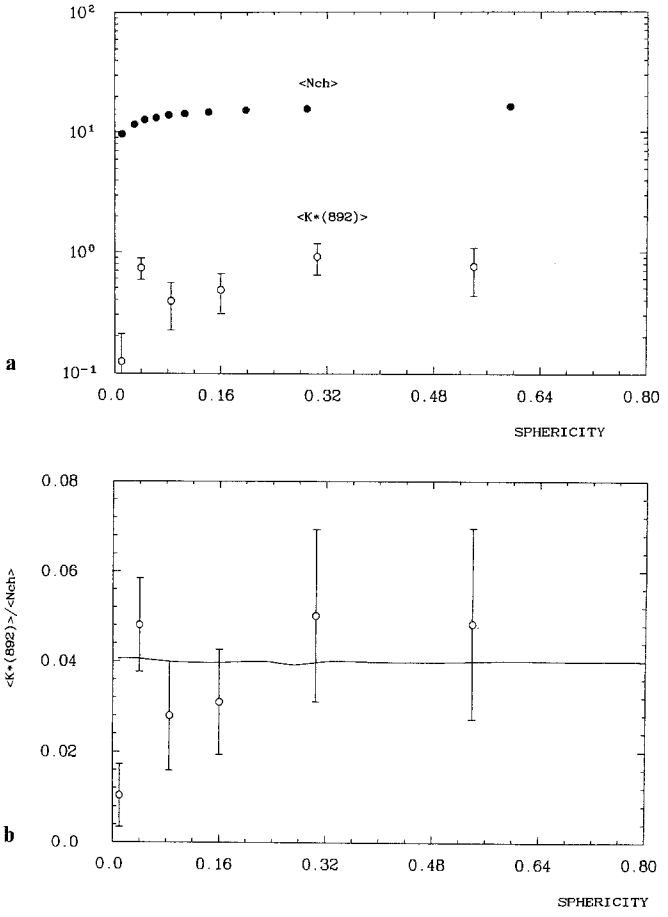


**Fig. 16. a** $K^{*\pm}(892)$ and total charged multiplicity as a function of event sphericity. **b** $K^{*\pm}(892)$ multiplicity relative to the total charged multiplicity as a function of event sphericity, along with a comparison with the Lund Monte Carlo, solid line

**Table 9.** $K^{*\pm}(892)$ multiplicity as a function of the event sphericity

| Sphericity | $\langle K^0\rangle$ | $\langle K^*\rangle/\langle n_{Ch}\rangle$ |
|---|---|---|
| 0.00–0.02 | $0.10\pm0.07$ | $0.010\pm0.007$ |
| 0.02–0.06 | $0.62\pm0.13$ | $0.048\pm0.010$ |
| 0.06–0.11 | $0.40\pm0.17$ | $0.028\pm0.012$ |
| 0.11–0.21 | $0.48\pm0.18$ | $0.031\pm0.012$ |
| 0.21–0.40 | $0.84\pm0.25$ | $0.050\pm0.019$ |
| 0.40–0.68 | $0.81\pm0.35$ | $0.048\pm0.021$ |

ment that the $K^0$ and charged pion forming a $K^*$ should belong to the same hemisphere, which could be dangerous for spherical events where the sphericity axis is not well determined.

## 4 Conclusions

We have measured differential and total cross sections for $K^0$ production at $\sqrt{s}=14.8$, 21.5, 34.5, 35 and 42.6 GeV and for $K^{*\pm}(892)$ production at $\sqrt{s}=34.5$, 35 and 42.6 GeV. Scale breaking effects have been measured. The $K^0$ and $K^{*\pm}(892)$ multiplicities per hadronic event have been obtained and compared and found to be in agreement with those published by other experiments. The strange meson production characteristics inside jets have been investigated. In particular their $p_t^2$ distributions show an exponential fall-off at low transverse momenta which can be described by the expression $Ae^{-p_t^2/2\sigma^2}$ with $\sigma\sim0.3$ GeV/c independent of energy. At high energies this exponential fall-off at low transverse momenta merges into a high transverse momentum tail. This is an indication that strange mesons are produced both in the quark and the gluon fragmentation. We have studied the strange meson yield as a function of event

sphericity. We have found a rise with increasing sphericity. The strange meson multiplicity relative to the total charge multiplicity is however flat with sphericity which we interpret as an indication that the strange meson content in gluon fragmentation is similar to that in quarks fragmentation.

*Acknowledgements.* We gratefully acknowledge the support of the DESY directorate, the PETRA machine group for high luminosity running and the staff of the DESY computer centres. Those of us from outside DESY wish to thank the DESY directorate for the hospitality extended to us.

## References

1. F. Barreiro: Habilitationsschrift, Fortschr. Phys. 34 (1986) 8
2. D. Saxon: Quark and gluon fragmentation in High Energy electron positron physics, A. Ali, P. Soeding (eds.). World Scientific, Singapore
3. A. Leites: D. Phil. Thesis (in preparation), Universidad Autonoma de Madrid
4. TASSO Coll. M. Althoff et al.: Z. Phys. C – Particles and Fields 27 (1985) 27
5. TASSO Coll. W. Braunschweig et al.: Z. Phys. C – Particles and Fields 45 (1989) 209
6. TASSO Coll. R. Brandelik et al.: Phys. Lett. 83 B (1979) 261
7. D. Cassel, H. Kowalski: Nucl. Instrum. Methods A 185 (1981) 235
8. D.M. Binnie et al.: Nucl. Instrum. Methods 228 (1985) 267
9. W. Schütte: Ph. D. Thesis, University of Hamburg, Interner Bericht, DESY-F1/84-03
10. TASSO Coll. R. Brandelik et al.: Phys. Lett. 113 B (1982) 499
11. TASSO Coll. R. Brandelik et al.: Z. Phys. C – Particles and Fields 39 (1988) 331
12. D.H. Saxon: Nucl. Instrum. Methods A 234 (1985) 258
13. SIMPLE program of B. Foster and S. Lloyd (unpublished)
14. F.A. Berends, R. Kleiss: Nucl. Phys. B 177 (1981) 141
15. P. Hoyer et al.: Nucl. Phys. B 161 (1979) 349
16. T. Sjostrand: Comp. Phys. Commun. 39 (1986) 347; B. Andersson, G. Gustafson, G. Ingelman, T. Sjostrand: Phys. Rep. 97 (1983) 33
17. R.J. Barlow: J. Comp. Phys. 72 (1987) 202
18. TASSO Coll. R. Brandelik et al.: Phys. Lett. 94 B (1980) 91
19. TASSO Coll. R. Brandelik et al.: Phys. Lett. 105 B (1981) 75
20. JADE Coll. W. Bartel et al.: Z. Phys. C – Particles and Fields 20 (1983) 187
21. PLUTO Coll. C. Berger et al.: Phys. Lett. 104 B (1981) 79
22. CELLO Coll. H.J. Behrend et al.: DESY-89-140
23. MARK II Coll. H. Schellman et al.: Phys. Rev. D 31 (1985) 3013
24. HRS Coll. M. Derrick et al.: Phys. Rev. D 35 (1987) 2639
25. TPC Coll. H. Aihara et al.: Phys. Rev. Lett. 53 (1984) 2378
26. R. Baier, K. Fey: Z. Phys. C – Particles and Fields 2 (1979) 339; G. Altarelli et al.: Nucl. Phys. B 160 (1979) 301
27. TASSO Coll. W. Braunschweig et al.: Z. Phys. C – Particles and Fields 42 (1989) 189
28. Particle Data Group, M. Aguilar-Benítez et al.: Phys. Lett. 204 B (1989) 1
29. JADE Coll. W. Bartel et al.: Phys. Lett. 145 B (1984) 441
30. HRS Coll. S. Abachi et al.: Phys. Lett. 199 B (1987) 151